THE LEBANESE AMERICAN UNIVERSITY

"Performance Enhancement of a Vertical Axis Wind Turbine using a Slotted Deflective Flap at the Trailing Edge"

By

Carla Attie

A thesis

Submitted in partial fulfillment of the requirements

for the degree of Master of Science in Mechanical Engineering

School of Engineering

July 2022

THESIS APPROVAL FORM

Student Name: Carla Mounir Attie   I.D. #: 201401809

Thesis Title: Performance Enhancement of a Vertical Axis Wind Turbine using a Slotted

Deflective Flap at the Trailing Edge

Program: Master of Science

Department: Mechanical Engineering

School: Engineering

The undersigned certify that they have examined the final electronic copy of this thesis and approved it in Partial Fulfillment of the requirements for the degree of:

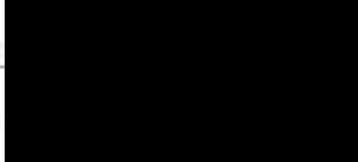Master of Science _____ in the major of Mechanical Engineering

Thesis Advisor's Name: Amne El Cheikh

Signature: ██████████   Date: 20 / 07 / 22
                                        Day   Month   Year

Committee Member's Name: Michel Khoury

Signature: ██████████   Date: 20 / 07 / 22
                                        Day   Month   Year

Committee Member's Name: Timmy Issa

Signature: ██████████   Date: 20 / 07 / 22
                                        Day   Month   Year

ii

THESIS COPYRIGHT RELEASE FORM

LEBANESE AMERICAN UNIVERSITY NON-EXCLUSIVE DISTRIBUTION LICENSE

Name: Carla Mounir Attie

Signature:

Date: 01 / 06 / 2022
      Day Month Year

PLAGIARISM POLICY COMPLIANCE STATEMENT

I certify that:

1. I have read and understood LAU's Plagiarism Policy.
2. I understand that failure to comply with this Policy can lead to academic and disciplinary actions against me.
3. This work is substantially my own, and to the extent that any part of this work is not my own I have indicated that by acknowledging its sources.

Name: Carla Mounir Attie

Signature: ■■■■■■■■■■■■■■■ Date: 01 / 06 / 2022
Day Month Year

Acknowledgment

Having the opportunity to work on this project would not have been possible without the support of many people.

 I offer my sincere appreciation for the patient advice and guidance throughout this research process provided by my thesis advisor, Dr. Amne El Cheikh. Her sincerity and motivation deeply inspired me throughout this process, and it was a great honor to study under her guidance.

I would like to thank Dr. Michel Khoury who provided invaluable guidance, counseling, and support. The completion of this study could not have been possible without his expertise.

A big thank you to Dr. Joelle Nader for her valuable contribution into this study. I am truly grateful for her dedication and expert role.

I would also like extend my appreciation to the engineering lab staff, especially Mr. Salim Jamal -Eddine, who were always prepared to assist with any technical issues I faced.

Finally, I am thankful for my loved ones, who encouraged and supported me through it all. The emotional support I received over the past two years was truly overwhelming and I could not have asked for a better support system.

Thank you all, for your unwavering support.

Performance Enhancement of a Vertical Axis Wind Turbine using a Slotted Deflective Flap at the Trailing Edge

Carla Attie

Abstract

Vertical axis wind turbines (VAWTs) exhibit dynamic stall under operational conditions which causes boundary layer separation from the surface of the blade. This hinders the turbine's overall performance in which the turbine displays low efficiency, aerodynamic losses, and vibration and noise generation. The aim of this study is to optimize the performance of an H-type Darrieus VAWT by employing a single-slotted deflective flap at the trailing edge of the blade. To optimize the turbine's performance, Computational Fluid Dynamics (CFD) and Design Of Experiments (DOE) methods are utilized simultaneously for time-saving purposes. The design parameters optimized for the NACA 0018 airfoil are the overlap (Δx), flap's gap (Δy), and deflection angle (δ_f). The influence of each parameter on the performance of the VAWT are determined by DOE, which yields the optimum combination of design parameters for this H-rotor VAWT as $\Delta x = 2$ mm, $\Delta y = 0.5$ mm, and $\delta_f = 9^0$ at TSR 3 where two-dimensional (2D) and three-dimensional (3D) CFD simulations yield turbine power increments of 27 % and 19 %, respectively. The flow characteristics of the 2D and 3D turbine models with slotted blades, developed using ANSYS Fluent R2020, demonstrated a delay in boundary layer separation and a reduction in vortices shedding due to the high-pressure flow through the slot, which in return reenergizes the boundary layer. The results from this study indicate an improved design of an H-rotor VAWT.

Keywords: Vertical Axis Wind Turbine, H Rotor, Slotted Deflective Flap, Computational Fluid Dynamics, Design of Experiments, Aerodynamic Performance

Computer Software

In this study, the simulations were generated using two commercial CFD software packages:

- ANSYS Fluent R2020 on an Intel Xeon E5-1630 v4 processor with 8 processors at a speed of 3.70 GHz and a RAM of 16 GB.
- ANSYS Fluent R2019 on an Intel Xeon E5-2650 v3 processor with 112 processors at a speed of 2.30 GHz and a RAM of 64 GB.

TABLE OF CONTENTS

LIST OF TABLES

LIST OF FIGURES

Nomenclature

A	Swept area, H.D [m^2]	$d\theta$	Azimuthal increment [^{0}]
c	Blade chord length [m]	H	Turbine height [m]
C_1	Top flap break [m]	n	Number of blades [-]
C_2	Bottom flap break [m]	p	Air density [kg/m^3]
C_f	Flap chord length [m]	R	Turbine radius [m]
C_m	Instantaneous moment coefficient	T	Thrust force [N]
C_p	Power Coefficient, $\lambda . C_m$ [-]	V_∞	Free stream velocity [m/s]
C_p/C_o	Turbine Performance [-]	λ	Tip speed ratio, $\omega . R/V_\infty$ [-]
d	Shaft diameter [m]	θ	Azimuth angle [^{0}]
D	Turbine diameter [m]	σ	Solidity, n.c/D [-]
dt	Time step [s]	ω	Rotational speed [rad/s]

Chapter I

Introduction

Glaciers are melting, sea levels are rising, heatwaves are destroying forests, and wildlife is going extinct. Global warming continues to rise as human beings power their modern lives with a strong dependence on fossil fuels. Scientists and engineers have devised ways to try to slow down global warming. One main advancement is the switch to harvesting energy from renewable resources. Renewable power systems are thriving, as this development reduces cost and promotes a cleaner future for generations to come.

Wind is one of the cheapest renewable resources available in many parts of the world. With abundant reserves in nature, wind power is considered one of the most promising and sustainable energy sources. In the year 2019, the global wind power market expanded by 19%, with 60 Gigawatts of new capacity added to the world's electric grids [1].

Wind energy is captured using a device known as a wind turbine, which then feeds an electric generator with mechanical rotational power to produce electricity. Lift-type wind turbines can be classified into horizontal axis wind turbines (HAWTs) and vertical axis wind turbines (VAWTs) depending on the orientation of the shaft relative to the ground, as illustrated in Figure 1.
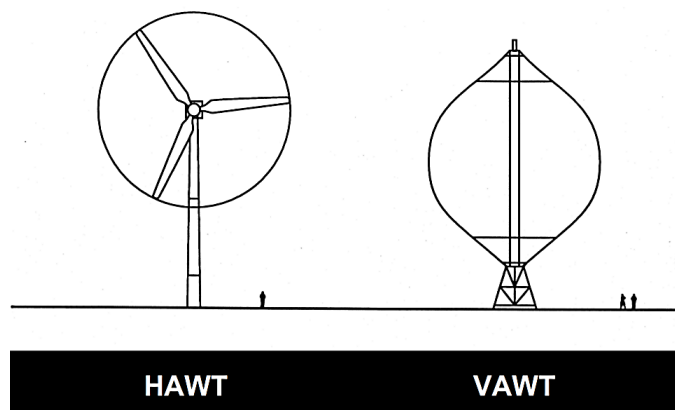
Figure 1: Schematic of HAWT vs VAWT

Today, HAWTs are more popular than their vertical counterparts in the wind energy market due to their higher efficiencies [2]. However, the VAWTs have recently grasped researchers' attentions due to their omni-directional capability, low noise

production, low installation and maintenance costs, and scalability[3]. Unfortunately, a VAWT still exhibits low efficiencies, aerodynamic losses, flow separation, and dynamic stall- all of which hinder the device's overall performance [4].

Flow separation is a critical factor that affects the aerodynamic performance of a wind turbine. The flow separation found from the blade surface of a wind turbine initially leads to a rapid decrease in the lift and then a sudden increase in the drag of the turbine blade [5]. Flow separation could increase the load on the wind turbine blade and reduce overall efficiency of the turbine[6]. Additionally, the fluid field in the region of flow separation is strongly unstable, which periodically generates separation vortices, leading to the vibration of rotating machinery and noise generation [7].

Based on the aforementioned issues, this study involves the numerical investigation of the best configuration of a single-slotted deflective flap located at the trailing-edge of a VAWT blade to delay or eliminate the boundary layer separation, which will enhance the overall aerodynamic performances of the Darrieus wind turbine, mainly the power coefficient (C_p). Since this is a lift turbine, the aerodynamic performances are all interdependent- as one aerodynamic parameter improves, so do the rest.

This study will have energy-saving benefits through the improvement of the VAWT's efficiency. Additionally, it will provide an upgrade in the wind energy market, creating a stride forward in the overall renewable energy industry.

The outline of this study is as follows: the background research is presented in Section 2, the aim and objectives of this study is described in Section 3, the geometrical and operational characteristics of the wind turbine, the computational settings, and the solution verification and validation analysis are described in Sections 4.1–4.2. The application of design of experiments (DOE) is defined in Section 5. The discussion and conclusions are detailed in Section 6-7.

Chapter II

Literature Review

To enhance the aerodynamic performances of VAWTs, extensive research has been conducted to improve the power coefficient of the turbine and to reduce the flow separation on the blades. To do this, VAWTs require flow-control techniques to enhance the flow fields on the blades. There are two flow techniques that can be implemented- namely, active flow control (AFC) and passive flow control (PFC) [8]. AFC's techniques consist of moving wall flow control technology, such as adding a rotating crossflow fan, but this technique adds many mechanical devices [9], which can be costly. On the other hand, PFC is a control mode without any external energy input, which makes it simple and easy to implement [10]. An example of a PFC technique is modifying the blade's airfoil shape.

Simple flap designs have been implemented in past studies and have proved to enhance the performance of VAWTs. Yang et al. [11] conducted a two-dimensional (2D) numerical analysis on a VAWT with a NACA0012 airfoil comprising a deflecting trailing-edge flap and analyzed the aerodynamic performances. Results showed that the flapped airfoil dampened the trailing-edge wake separation, deferred the dynamic stall, reduced the oscillating amplitude, and with the flap control, the peak power coefficient increased by 10% relative to the baseline turbine[11]. Liu et al. investigated the effects of trailing-edge flap on the aerodynamic performance and noise characteristics of a VAWT employing the NACA0018 airfoil blade profile [7]. The research results indicated that the trailing-edge flap effectively suppressed flow separation and reduced the generated noise at high angles of attack [7]. Similarly, Zhu et al. analyzed the performance of a VAWT subjected to three types of flow-deflecting-gaps (FDGs), which included two-side FDG blade, toward-outside FDG blade and toward-inside FDG blade [4]. The obtained results indicated that the FDG enhanced the stalling angle of attack by 2°, increased the glide ratio, decreased the frequency of vortex shedding, and greatly reduced the amplitude of lift oscillation [4]. Moreover, the jet flow in FDG towards the leading edge offset the swirling flow over the suction surface [4]. Likewise, Mohamed et al. examined the effect of employing a slotted NACA0018 airfoil on the turbine blade and analyzed the performance of a VAWT, and it was noted that the slotted airfoil delayed flow

separation at high angles of attack and improved the power coefficient at low tip speed ratios (TSRs) [12].

Aircraft blades have been subjected to much more complex flap designs when compared with VAWT blades and have shown greater performance improvements. Sforza noted that the implementation of a double slotted flap at the trailing edge of an aircraft's airfoil increases the lift coefficient, power coefficient, and decreases the starting torque [13]. Florjancic implemented a single-slotted flap to an existing high lift system in general aviation aircraft [14]. The resulting single-slotted flap design improved the maximum lift coefficient by 27% with respect to the original plain flap [14]. Similarly, Weishung et al. introduced the flexible variable camber trailing-edge flap on aircraft winglets [15]. It was noted that the flap helped to improve the glide ratio over a wide range of lift coefficients, and the maximum lift enhancement was about 30% [15].

In review, the previous studies on VAWTs mostly focus on investigating the effects of adding a specific trailing edge flap to control the flow under explicit conditions. In other words, the geometric parameters of the flap's design were not critically analyzed. Also, the flap designs implanted on the VAWTs were very simple, whereas for aircrafts, the flap designs were much more complex with greater attention to detail and produced better improvements in the aerodynamic performances.

Consequently, this study entails the design of a single-slotted deflective flap, inspired by Florjancic's design implemented on aircrafts [14], located at the trailing-edge of a VAWT airfoil. Moreover, it involves the analysis of an H-type Darrieus VAWT aerodynamic performances, mainly that of the power coefficient, and a detailed study of the flow field around the blades using numerical simulations. The best design, which optimizes the turbine's performance and decreases flow separation, has been evaluated and highlighted under Section 5.

Chapter III

Aim & Objectives

With the use of numerical simulations, the aim of this study was to design an optimal single-slotted deflective flap located at the trailing-edge of a VAWT blade to enhance the turbine's power coefficient and to delay the flow separation around the blades.

To achieve this, a 2D VAWT model was constructed as the baseline turbine. Since many geometric parameters control the shape of the flap and its location on the blade, DOE was utilized to reduce the required number of simulations. Then computational fluid dynamics (CFD) simulations were generated on the baseline and flapped turbines to analyse their performances. The flapped design with the greatest enhancement effect on the coefficient of performance of the turbine was chosen. It is worth noting that simplified 2D CFD simulations involve errors associated with neglecting the tip effects, but with the benefit of reducing computational time significantly. Therefore, three-dimensional (3D) CFD simulations on the final selected design was applied to validate the study further.

Chapter IV

Methodology

4.1 The Physical Model & Scope of Design

The reference turbine model used in this study is that of Tescione et al. [16], and the fluid domain limits are set based on the recommendations of Rezaeiha et al. [17] who devised accurate domain limits for CFD simulations of VAWTs at different TSRs and solidities using the same model as that of Tescione et al. The reference turbine consists of an H-rotor VAWT with symmetrical NACA0018 blades and a chord length (c) of 0.06m. The turbine's diameter (D) is 1 m and the shaft's diameter (d) is 0.04 m. The turbine rotates counterclockwise in a freestream velocity (V_∞) of 9.3 m/s. The reference turbine's tip speed ratio (λ) is 4.5, and referring to Eq. (1), this leads to a rotational speed (ω) of 83.8 rad/s. The solidity (σ), calculated using Eq. (2), is 0.12.

$$\lambda = \frac{\omega R}{V_\infty} \tag{1}$$

$$\sigma = \frac{nc}{D} \tag{2}$$

The features of the reference turbine model by Tescione et al. [16] are shown in Figure 2 detailed in Table 1. The blade orbit is divided into four quartiles as [18]: ($45^0 \leq \theta < 135^0$) upwind, ($135^0 \leq \theta < 225^0$) leeward, ($225^0 \leq \theta < 355^0$) downwind, ($315^0 \leq \theta < 45^0$) windward. Where θ is the azimuth angle of the turbine blade.
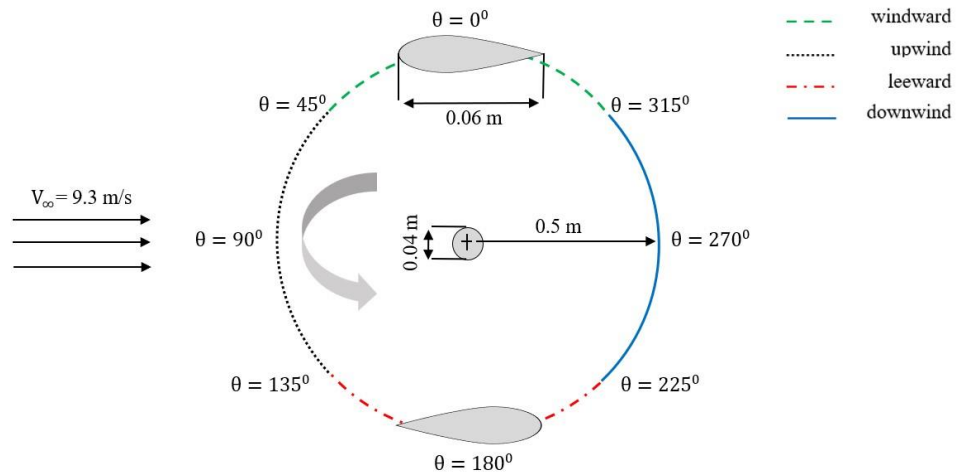
Figure 2: Schematic of reference turbine (not to scale)

Table 1 Characteristics of the reference VAWT inspired by Tescione et al. [16]

Parameter	Value
Airfoil	NACA0018
Turbine Diameter, D [m]	1
Shaft Diameter, d [m]	0.04
Chord Length, c [m]	0.06
Number of Blades, n	2
Tip Speed Ratio, λ [-]	1.5 - 4.5
Freestream Velocity, V_∞ [m/s]	9.3
Rotational Speed, ω [rad/s]	27.9 - 83.8
Swept Area, A [m^2]	1
Solidity, σ [-]	0.12

The flapped geometry's design parameters, inspired by Florjancic's design implemented on aircraft wings [14], are presented in Figure 3. The well-known and widely used H-type VAWT was selected, with symmetrical NACA0018 airfoils as the blade cross-section. The airfoil's total chord length is fixed ($c = C + C_f = 0.06$ m). Similarly, the flapped section of the airfoil is one of an inflexible size, consisting of the flap's chord length ($C_f = ¼ c$), the top flap break ($C_1 = 0.9 c$) and the bottom flap break ($C_2 = 0.75 c$). A b-spline curve (b) constructed from six points has been employed to design the flap according to specified geometric constraints. The parameters which were altered and studied are the flap's overlap (Δx), the flap's gap (Δy), and the flap's deflection angle (δ_f).
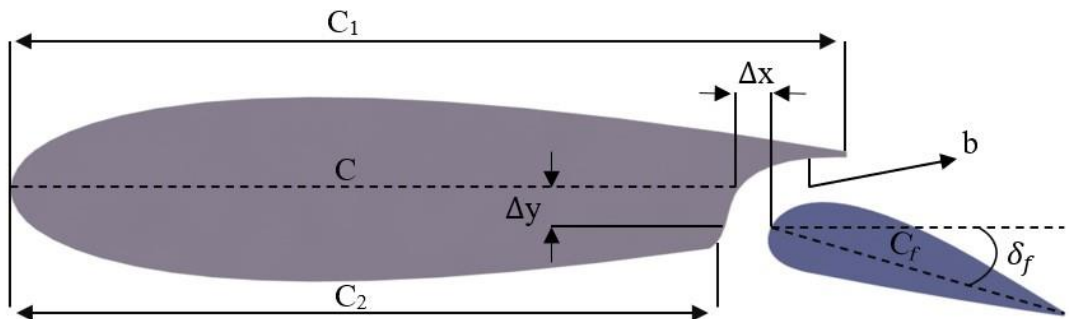
Figure 3: Schematic diagram of the single-slotted flapped airfoil

The pressure difference between both ends of the slot causes a jet flow through it, generating a high momentum flow injected into the boundary layer on the upper surface. The purpose of this jet is to delay the flow separation and subsequently improve the turbine's power coefficient.

4.2 Computational Fluid Dynamics

The aerodynamic performance of each model was analyzed using the commercial CFD software package ANSYS Fluent R2020.

The power coefficient was generated through a dimensionless analysis using the instantaneous moment coefficient (C_m) and TSR (λ). C_m was found using ANSYS Fluent Postprocessing. Using dimensional analysis, C_p is derived as follows:

$$C_m = \frac{T}{\frac{1}{2}\rho V_\infty^2 AR} \tag{3}$$

Where T is the torque acting on the rotor in N-m, ρ is the air density in kg/m³, V_∞ is the wind velocity in m/s, A is the rotor's swept area in m² and R is the rotor radius in m.

$$C_P = \frac{T\omega}{\frac{1}{2}\rho V_\infty^3 A} \tag{4}$$

From equations (1), (3) and (4), the power coefficient is:

$$C_P = \lambda C_m \tag{5}$$

4.2.1 Computational Domain

Appropriate domain sizing was needed to ensure reliable results. A schematic of the computational domain, as proposed by Rezaeiha et al. [17], is shown in Figure 4. The domain dimensions are presented in terms of the turbine's diameter. The turbine is located 15 D from the inlet boundary and 15 D from the outlet boundary to ensure a full development of the wake in the downstream region. The inlet is 20 D wide, and the rotor is placed within a rotating domain of 1.5 D. A sliding mesh interface is used to merge the stationary and rotating fluid domains into a single zone to ensure a continuous flow.
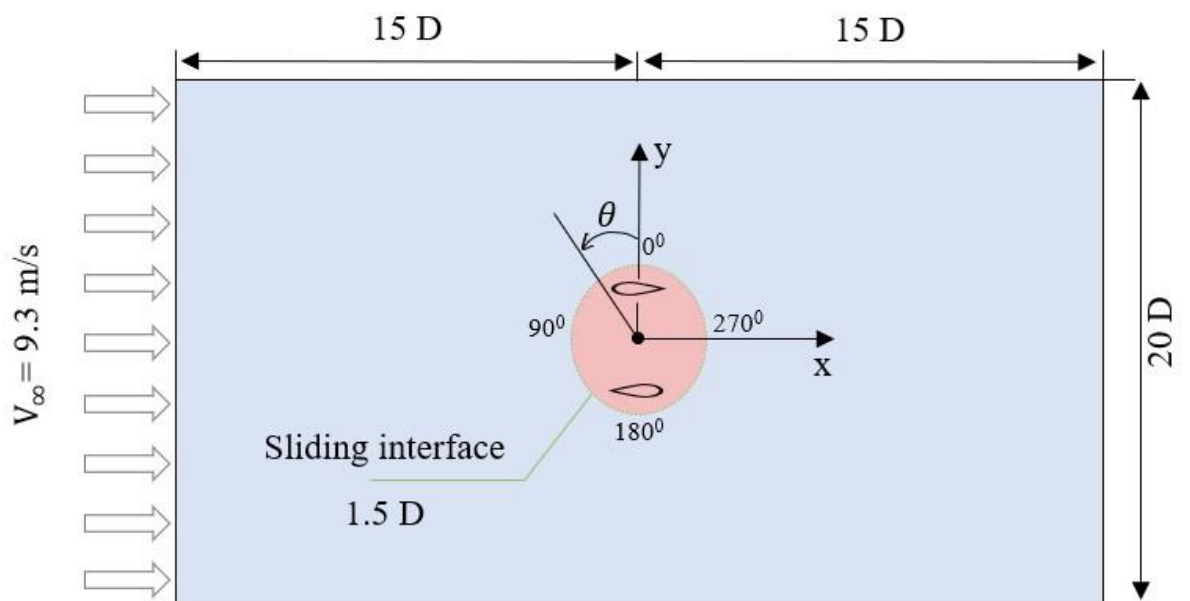
Figure 4: Schematic of computational domain (not to scale)

4.2.2 Computational Grid

(a) Mesh distribution near the rotating core

(b) Mesh distribution near the subzone

(d) Mesh distribution near the trailing edge

(c) Mesh distribution near the airfoil

(e) Flapped airfoil mesh distribution
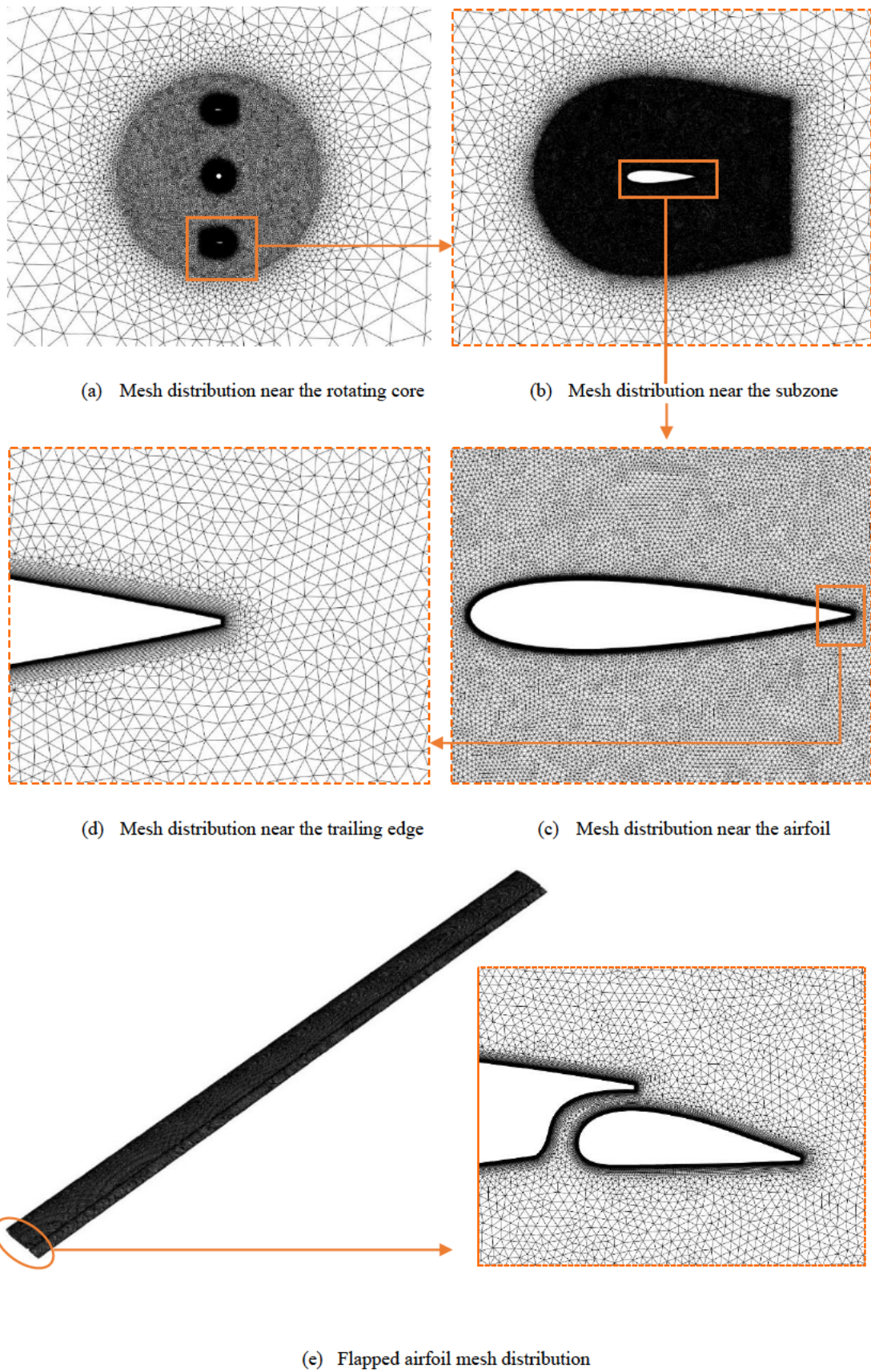
Figure 5: Computational grid

High-quality meshing was crucial to guarantee reliable results. The computational grid, shown in Figure 5, consists of approximately 450,000 elements for the 2D model and 11.6 million elements for the 3D model. For all cases, the computational grid is made up of triangular cells. The cell size is equal on both sides of every interface (between the rotating domain and the stationary fluid domain and between the subzones and the rotating domain as well) to control numerical errors at these interfaces. The cell size on each blade surface is 1.8×10^{-4} m, and 30 inflation layers with a total thickness 9×10^{-4} m was applied. The maximum y^+ value around the turbine is ≈ 1, the maximum skewness is ≈ 0.68 and the minimum orthogonal quality is ≈ 0.3.

4.2.3 Numerical Model

Working with the ANSYS Fluent R2020 solver on the 2D models and ANSYS Fluent R2019 on the 3D models, transient pressure-based simulations were generated on each model. The k-ω SST turbulence model was applied for a more accurate near-wall treatment[19]. The physical properties of the fluid air surrounding the turbine are mainly its density and dynamic viscosity taken as $\rho = 1.225$ kg/m^3 and μ =1.7894x10^{-5} kg/m.s, respectively. The sliding mesh approach was adopted where the rotating body was set to mesh motion with a counterclockwise angular velocity based on the value of TSR. The boundary conditions were set as follows: $V_\infty = 9.3$ m/s at the inlet, a constant gauge pressure at the outlet, and stationary non-slip conditions on the turbine walls. The pressure-velocity coupling algorithm was set as Semi-Implicit Method for Pressure Linked Equations (SIMPLE), and the second order upwind discretization scheme was implemented for all unsteady Reynolds Averaged Navier-Stokes (URANS) equations to ensure minimum numerical diffusion. An azimuthal angle increment (dθ) of 0.1^0 per timestep was adopted after having conducted a timestep sensitivity analysis, detailed under Section 4.2.4. The calculations utilize 20 iterations per timestep. The solution converges when scaled residuals of all equations fall below 1e^{-5}.

4.2.4 Solution Verification & Validation

4.2.4.1 2D Model Verification

To verify the results, two important studies were conducted, namely the grid sensitivity study and the timestep sensitivity study. With a grid sensitivity study, as the density of the grid increases, the more stable the instantaneous moment coefficient tends to be just as predicted in Figure 6, which shows the variation of C_m with four different grid sizes for the 2D model. The grid size for each mesh type presented in Figure 6 and the turbine's corresponding maximum y^+ values are detailed under Table 2. The mesh report discussed in Section 4.2.2 is highlighted as Mesh 3, which consists of approximately 450,000 elements. On the contrary, with a timestep sensitivity study, as the lower the value of the azimuthal angle increments per timestep decrease, the more stable the instantaneous moment coefficient tends to be as shown in Figure 7, which predicts the variation of C_m with four different azimuthal increments per timestep for the 2D model. It was noted by Rezaeiha et al.'s analysis that for relatively high TSRs (TSR 4.5 – 5.5), the instantaneous moment coefficient was negligible for $d\theta \leq 0.5^0$ [17]. However, since this study included simulations generated for TSR values 2 – 4, both the grid sensitivity and timestep sensitivity studies were conducted at a TSR of 1.5. As mentioned in Section 4.2.3, $d\theta$ was set to 0.1^0 because, as shown in Figure 7, the solution was stable at $d\theta = 0.1^0$ for a TSR of 1.5.
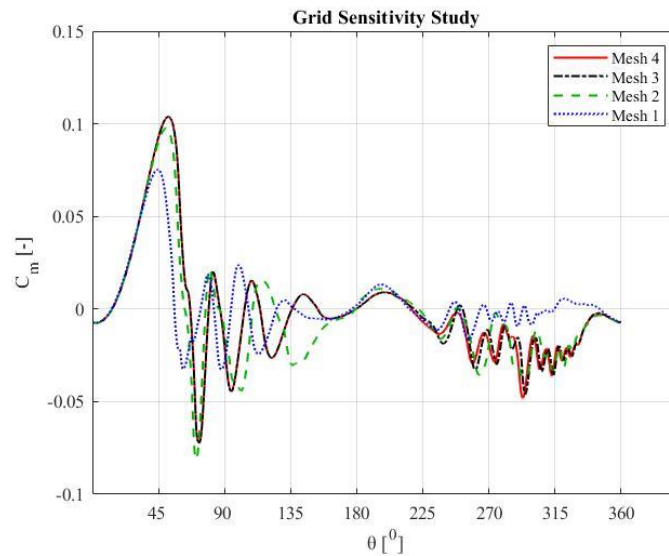
Figure 6: 2D model instantaneous moment coefficient for four grids at TSR 1.5

Table 2 2D Grid specifications

Grid type	Number of elements (approx..)	Corresponding maximum y^+
Mesh 1	150,000	3.3
Mesh 2	300,000	2.4
Mesh 3	450,000	≈ 1
Mesh 4	600,000	< 1
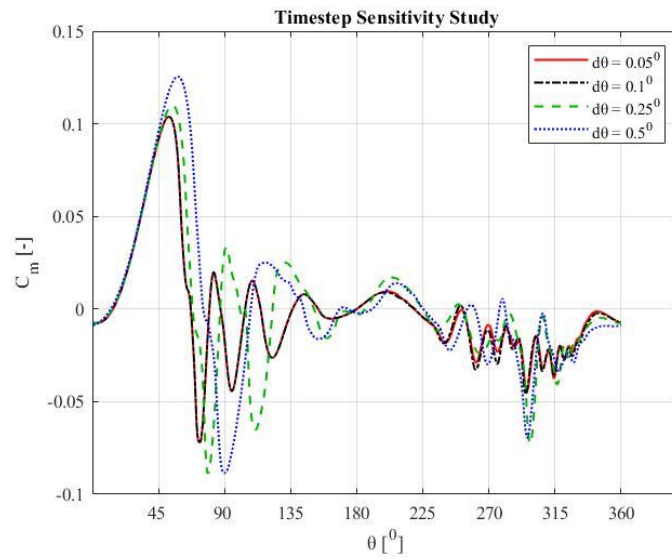
Figure 7: 2D model instantaneous moment coefficient for four azimuthal increments at TSR 1.5

4.2.4.2 3D Model Verification

The verification of the 3D model involved the same procedure as that of the 2D model. However, the verification study was conducted at a TSR of 3 since the optimized slotted flap design was found at this tip speed ratio (detailed under Section 6). As predicted in Figure 8, which illustrates the variation of C_m with three different grid types for the 3D model, the solution can be considered stable after applying the 'Medium' grid setup. The grid size for each mesh type presented on Figure 8 and the turbine's corresponding maximum y^+ values are detailed under Table 3. As presented in Figure 9 which predicts the variation of C_m with three different azimuthal increments per timestep for the 3D model, the solution converged at $d\theta = 0.1^0$.

Table 3 3D Grid specifications

Grid type	Number of elements (approx..)	Corresponding maximum y^+
Coarse	7.67 million	2.1
Medium	11.6 million	≈ 1
Fine	14.6 million	< 1
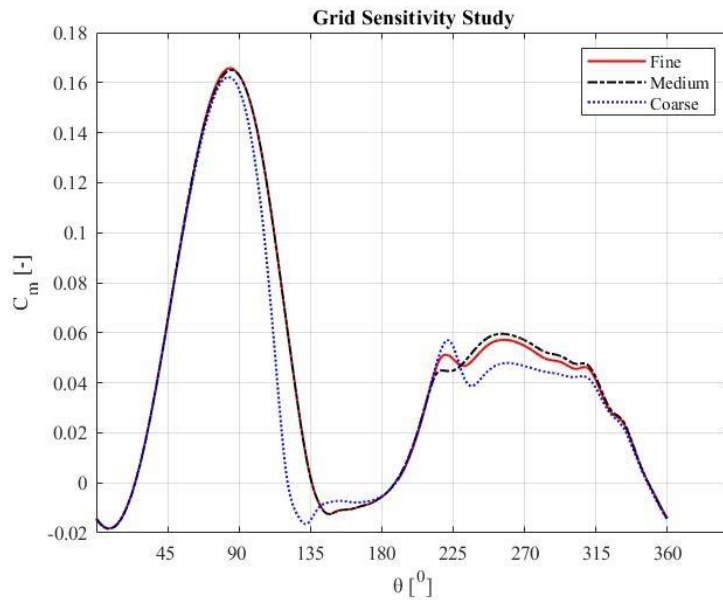
Figure 8: 3D model instantaneous coefficient for three grids at TSR 3
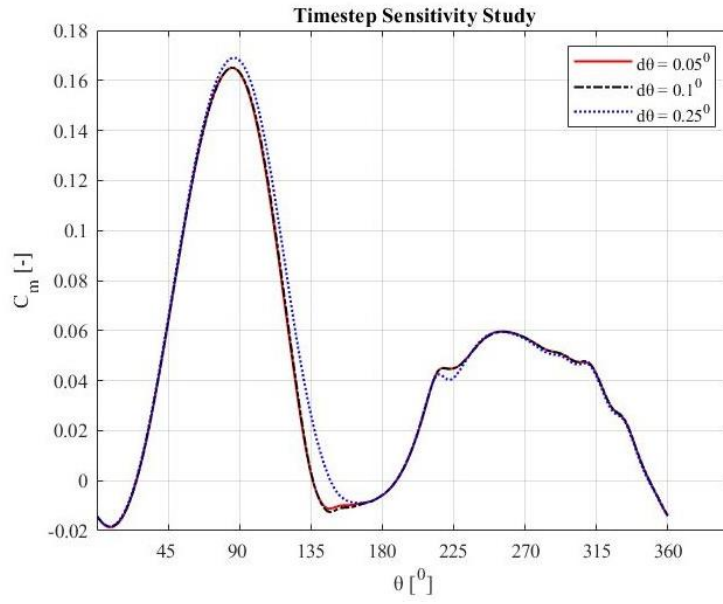
Figure 9: 3D model instantaneous moment coefficient for three azimuthal increments at TSR 3

4.2.4.3 Validation

The validation study on the 2D and 3D models included a comparative analysis of the streamwise normalized velocities at x = 2R and x = 3R at TSR of 4.5 between the CFD simulation results and the experimental results obtained by Tescione et al. [16]. The results from this analysis are shown on Figure 10. The comparison of the time-averaged normalized streamwise velocities at x = 2R and x = 3R showed a deviation of 6.3-18.1% for the 2D model and a deviation of 8.1-21.8% for the 3D case. This difference can be due to the turbulence model used in this study, but higher models like large eddy simulation (LES) and detached eddy simulation (DES) are cost ineffective as they require higher computational time.
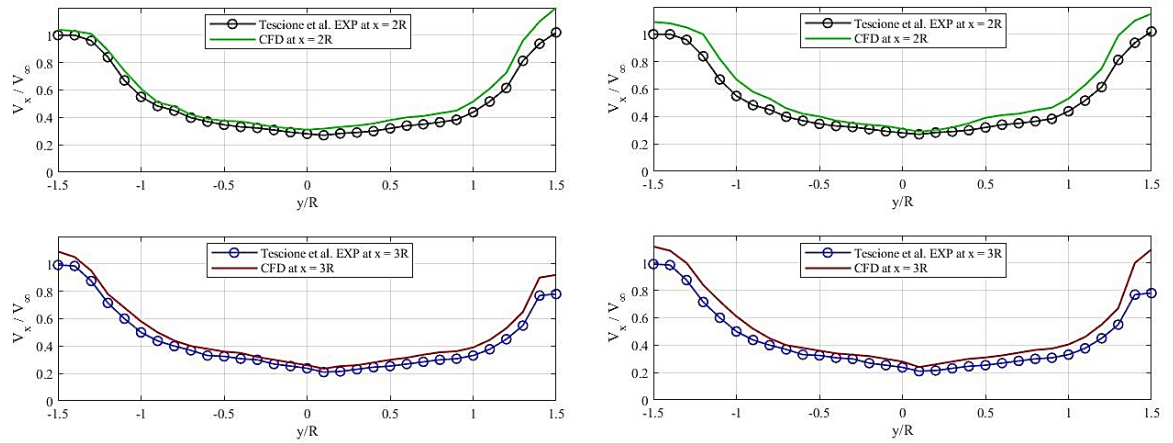
Figure 10: Normalized streamwise velocity at x = 2R & x = 3R at TSR 4.5 for the 2D (left) and 3D (right) models

Chapter V

Design of Experiments

5.1 Introduction to the DOE Approach

The design and optimization of wind turbines usually involves a parametric study with multiple runs to examine the effect of various parameters on the turbine performance. Whether the study is experimental or numerical, performing the full factorial design is usually costly and time-consuming. For example, a full factorial design of 4 factors having 5 levels each requires 4^5 or 1024 runs. Therefore, recent studies in various engineering fields are employing the orthogonal design of experiments approach to reduce the number of runs required to estimate the influence of the factors on the response and the optimal combination of factors to maximize/minimize the response. In the wind turbine research area, DOE methodology became more popular to optimize various wind turbine configurations [20–28]. Wang et al. employed Taguchi's method to numerically optimize the aerodynamic performance of a three-bladed VAWT with leading edge serrations[20]. The VAWT with optimum geometric configuration of amplitude, wavelength and twist angle of the serrations was found to yield 18.3% increase in the power output compared to the baseline turbine. Moreover, Zhang et al. used an orthogonal DOE array to determine the effect of six geometric parameters, controlling a winglet shape, on the performance of a wind turbine with winglet attached at its tip [26]. By decreasing the tip vortices effect, the optimum winglet configuration helps in increasing the blade's power by up to 31%. A similar approach was adopted by Ahmad et al. to optimize the geometric parameters of the inner turbine in a double-Darrieus hybrid turbine [22]. The combination of optimum number of blades, blade chord length, pitch angle, rotor height and distance of inner turbine from the shaft not only enhanced its power extraction capability, but also reduced the cut-in speed. Therefore, the proposed hybrid configuration is more suitable for locations with low wind speeds than conventional Darrieus turbines. In the coming section, details of the orthogonal DOE used in this study will be presented.

5.2 Experimental Design and Statistical Analysis

Aiming at accurately and effectively studying the impact of influencing parameters, then modelling, optimizing, and validating the generated models, a lean six sigma advanced statistical tool was adopted using the Response Surface Methodology, a renowned simulation modelling tool.

At a primary stage, the most influencing design parameters on turbine performance were assessed and their ranges of variability were examined. The latter were identified following a series of preliminary trials based on changing one factor at a time while keeping others constant.

Based on this preliminary analysis, the most influencing operating variables were the flap's overlap (Δx), flap's gap (Δy), the flap's deflection angle (δ_f), and the tip speed ratio (TSR). Δx ranged from 1 to 3 mm, Δy from 0.5 to 2.5 mm, while δ_f varied between 0 and 30 degrees and TSR between 2 and 4. These four independent variables (Δx, Δy, δ_f, TSR) with their five levels are shown in Table 4 in their coded and real values.

Table 4 Levels of independent operating parameters used for the central composite rotatable design.

Operating Variables	Symbol	Coded Values				
		$-\alpha^*$	-1	0	$+1$	$+\alpha^*$
Flap's overlap	Δx	1	1.5	2	2.5	3
Flap's gap	Δy	0.5	1	1.5	2	2.5
Flap's deflection angle	δ_f	0	7.5	15	22.5	30
Tip speed ratio	TSR	2	2.5	3	3.5	4
With α (star point) = 2						

A central composite rotatable design (2^4) factorial design with 6 repetitions at the central level and 8 axial points (where one variable is set at an extreme level (± 2) while other variables are set at their central points) was adopted. A total of 30 experiments were generated, and the corresponding experimental design indicating the levels of the turbine operating variables and the values of the response parameter (the turbine performance (C_p/C_o)) is shown in Table 5.

Table 5 Experimental design showing the levels of turbine operating variables and the values of C_p/C_o response parameter for the 30 runs.

RN	Coded levels (OP)				Actual Values (OP)					Response (RP)
	X_1	X_2	X_3	X_4	X_1	X_2	X_3	X_4	DP	Y
1	-1	-1	-1	-1	1.5	1	7.5	2.5		1.1233
2	+1	-1	-1	-1	2.5	1	7.5	2.5		1.1588
3	-1	+1	-1	-1	1.5	2	7.5	2.5		0.9549
4	+1	+1	-1	-1	2.5	2	7.5	2.5		1.0430
5	-1	-1	+1	-1	1.5	1	22.5	2.5		0.6047
6	+1	-1	+1	-1	2.5	1	22.5	2.5	2^4 Factorial Design Points	0.6626
7	-1	+1	+1	-1	1.5	2	22.5	2.5		0.3293
8	+1	+1	+1	-1	2.5	2	22.5	2.5		0.4570
9	-1	-1	-1	+1	1.5	1	7.5	3.5		1.0901
10	+1	-1	-1	+1	2.5	1	7.5	3.5		1.1046
11	-1	+1	-1	+1	1.5	2	7.5	3.5		1.0201
12	+1	+1	-1	+1	2.5	2	7.5	3.5		1.0329
13	-1	-1	+1	+1	1.5	1	22.5	3.5		0.7439
14	+1	-1	+1	+1	2.5	1	22.5	3.5		0.7590
15	-1	+1	+1	+1	1.5	2	22.5	3.5		0.5773
16	+1	+1	+1	+1	2.5	2	22.5	3.5		0.6277
17	-2	0	0	0	1	1.5	15.0	3		1.0838
18	+2	0	0	0	3	1.5	15.0	3		1.1407
19	0	-2	0	0	2	0.5	15.0	3		1.2632
20	0	+2	0	0	2	2.5	15.0	3	Star Points	1.0193
21	0	0	-2	0	2	1.5	0.0	3		0.9975
22	0	0	+2	0	2	1.5	30.0	3		0.5617
23	0	0	0	-2	2	1.5	15.0	2		0.0001
24	0	0	0	+2	2	1.5	15.0	4		0.6953
25	0	0	0	0	2	1.5	15.0	3		1.1315
26	0	0	0	0	2	1.5	15.0	3		1.1315
27	0	0	0	0	2	1.5	15.0	3	Central Level Points	1.1315
28	0	0	0	0	2	1.5	15.0	3		1.1289
29	0	0	0	0	2	1.5	15.0	3		1.1377
30	0	0	0	0	2	1.5	15.0	3		1.1383

RN: Run Number; OP: Operating Parameter; DP: Design Points; RP: Response Parameter.
X_1: flap's overlap (Δx in mm); X_2: flap's gap (Δy in mm); X_3: flap's deflection angle (δ_f in degrees); X_4: tip speed ratio (TSR, no unit); Y: Turbine Performance (C_p/C_o)

In this analysis, C_o is the power coefficient of the baseline turbine and C_p is the power coefficient of the slotted turbine.

Collected data were processed and treated using the analysis design procedure of Statgraphics Centurion 18 (Version 18, Windows XP) and advanced statistics were generated. These analyses included the analysis of variance (ANOVA), an empirical modelling using polynomial regression analysis, and finally an optimization and validation procedure. The statistical significance of each parameter at 5 % risk level was estimated by the 2-way ANOVA test and was portrayed by the Pareto charts of standardized effects presented on Figure 11.

A nonlinear second-degree polynomial equation (Eq. (6)) was fitted in each response to describe the process empirically.

$$Y = a_0 + \sum_{i=1}^{k} a_i x_i + \sum_{i=1}^{k-1} \sum_{j=i+1}^{k} a_{ij} x_i x_j + \sum_{i=1}^{k} a_{ii} x_i^2 \tag{6}$$

Where, a_0, a_i, a_{ii} and a_{ij} are the regression coefficients, x_i and x_j are the coded levels of independent variables and k is the number of operating parameters.

The coefficient of determination (R^2) relative to this equation reflects the percentage of the variability in C_p/C_o explained by the model as fitted.

Response surfaces were also generated and plotted between two significant variables while the third was fixed at the optimal level as shown in Figures 12 and 13. A projection of the response surface on a two-dimensional base shows the iso-response curves that make it easier to predict responses within the selected range of variables and to detect the optimal region as illustrated on Figure 14. The optimization of turbine performance aimed at finding the most appropriate and workable optimal combination of levels of Δx, Δy, δ_f, and TSR, which could maximize the C_p/C_o value.

Chapter VI

Results & Discussion

6.1 Effects of Turbine Design Variables (Δx, Δy, δ_f, TSR) on its Overall Performance

A two-way ANOVA with interaction was carried out to identify significant effects (with p-value < 0.05, at 95% confidence level) of the studied parameters within the previously identified ranges of variability. The ANOVA table, shown as Table 6, partitions the variability in C_p/C_o into separate pieces for each of the effects. It then tests the statistical significance of each effect by comparing the mean square against an estimate of the experimental error. In this case, five effects have P-values less than 0.05, indicating that they are significantly different from zero at the 95.0% confidence level.
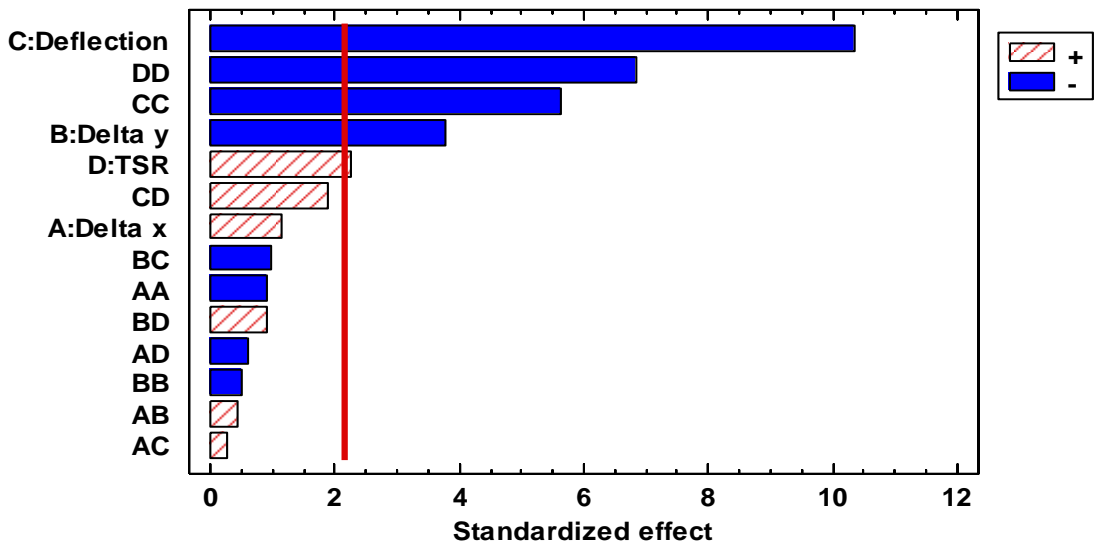
Figure 11: Standardized Pareto Chart for Cp/Co showing the significant linear, quadratic and interaction effects.

In effect, the analysis of variance clearly shows that within the tested ranges, δ_f had the most significant linear effect (*p-value 0)* followed by the linear effects of Δy and TSR with p-values of 0.002 and 0.04, respectively. Additionally, δ_f and TSR showed significant quadratic effects *(p-values ~ 0).* The level of significance along with the sign of each effect (positive or negative) were also portrayed by the aspect and color of the bar charts surpassing the vertical red line that indicates the 95% confidence

level in the Pareto chart presented in Figure 11. All significant effects were negative except for TSR which was positive. No significant interaction effects were identified.

Table 6 Analysis of Variance for C_p/C_o

Source	Sum of Squares	Df	Mean Square	F-Ratio	P-Value
A: Δx	0.0110963	1	0.0110963	1.33	0.2679
B: Δy	0.119358	1	0.119358	14.32	0.0020
C: δ_f	0.896219	1	0.896219	107.53	0.0000
D: TSR	0.0425441	1	0.0425441	5.10	0.0403
AA	0.00699347	1	0.00699347	0.84	0.3752
AB	0.00152116	1	0.00152116	0.18	0.6757
AC	0.0006251	1	0.0006251	0.08	0.7882
AD	0.00292892	1	0.00292892	0.35	0.5628
BB	0.00213334	1	0.00213334	0.26	0.6208
BC	0.0077855	1	0.0077855	0.93	0.3502
BD	0.0066271	1	0.0066271	0.80	0.3876
CC	0.263217	1	0.263217	31.58	0.0001
CD	0.0294545	1	0.0294545	3.53	0.0811
DD	0.390813	1	0.390813	46.89	0.0000
Total error	0.116683	14	0.00833448		
Total (corr.)	1.84923	28			

R-squared = 93.6902 percent

R-squared (adjusted for Df.) = 87.3804 percent

Standard Error of Est. = 0.0912934

Mean absolute error = 0.0448075

Durbin-Watson statistic = 1.79962 (P = 0.1236)

Lag 1 residual autocorrelation = 0.0949196

In fact, the best performance was noticed at low flap's deflection angles and while increasing the deflection from 0 to 30 degrees, the wind turbine performance drastically decreased, as depicted on Figure 12. As for the flap's gap, it showed a

slight negative effect on C_p/C_o but the performance was always improved within the tested range of variability. Finally, as shown in the trends of estimated response surfaces (Figures 12 and 13), TSR had a significant positive linear effect with a clearly noticeable negative quadratic effect on turbines' performance with the best C_p/C_o being achieved at a TSR of around 3. Beyond this level of TSR, C_p/C_o will follow again a decreasing pattern while reaching a value that is significantly greater than the performance achieved at very low TSR levels.
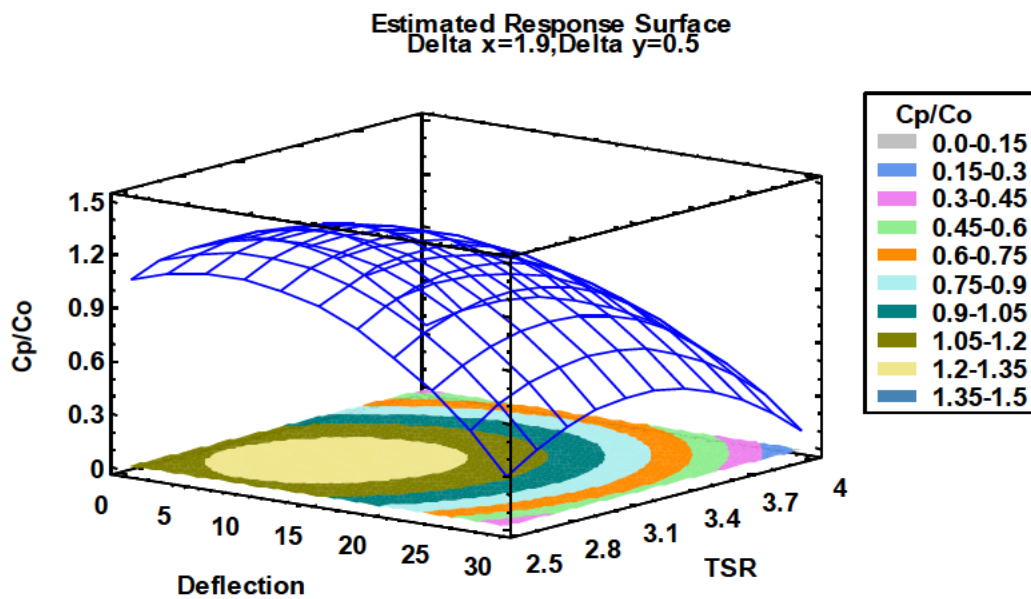

Figure 12: Three-dimensional estimated response surface of Cp/Co as a function of the deflection angle and TSR when Δx and Δy are set at their optimal level.
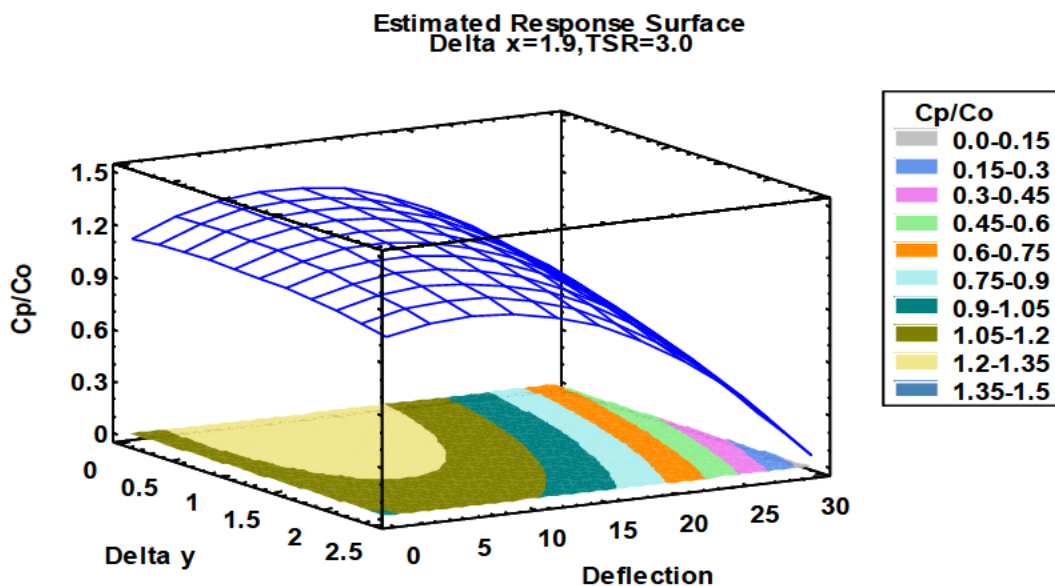

Figure 13: Trend of the estimated response surface of Cp/Co as a function of the deflection angle and Δy when Δx and TSR are set at their optimal level.

25

6.2 Model Fitting and Validation

The relationship between the wind turbine's performance reflected by C_p/C_o values and the independent turbine's operating variables was examined by means of the multiple regression method. Suitable regression coefficients were estimated using the method of least squares based on minimizing the sum of the squared residuals. The second-order polynomial equation that was fitted to C_p/C_o response parameter came as follows:

$$
\begin{aligned}
C_p/C_o = {} & -4.42584 + (0.3810 * \Delta x) - (0.2677 * \Delta y) - (0.0016 * \delta_f) \\
& + (3.6650 * \text{TSR}) - (0.0648 * \Delta x^2) + (0.0390 * \Delta x * \Delta y) \\
& + (0.0017 * \Delta x * \delta_f) - (0.0541 * \Delta x * \text{TSR}) \\
& - (0.0358 * \Delta y^2) - (0.0059 * \Delta y * \delta_f) \\
& + (0.0814 * \Delta y * \text{TSR}) - \left(0.0018 * \delta_f{}^2\right) \\
& + (0.0114 * \delta_f * \text{TSR}) - (0.6252 * \text{TSR}^2)
\end{aligned}
\tag{7}
$$

The reported coefficient of determination R-squared statistic of C_p/C_o (shown in Table 6 was high and indicates that the model as fitted explains 93.69% of the variability in C_p/C_o. The adjusted R-squared statistic, which is more suitable for comparing models with different numbers of independent variables, is 87.38%. As for the Durbin-Watson (DW) statistic (shown in Table 6), it tests the residuals to determine if there is any significant correlation based on the order in which they occur. Since the P-value is greater than 5.0%, there is no indication of serial autocorrelation in the residuals at the 5.0% significance level.

On the other hand, the differences between the observed values and model's predicted (fitted) values were small (did not exceed the mean absolute error) and unbiased. This was concluded after validation (shown in Table 7) of the generated model at different combinations of levels of the operating variables including the optimal point that will be detailed in the following section and other points that were not exploited in the initial design. It can be then summarized that RSM model equation had a high goodness of fit and could be effectively used to estimate the improvement in turbine's performance as compared to the baseline (reflected by C_p/C_o values) at any possible combination of Δx, Δy, δ_f, and TSR values within the test range

26

Table 7 Model validation: comparison between fitted and numerical response values at the optimal conditions (highlighted in red) and other levels of combinations randomly chosen within the test range.

Δx	Δy	δ_f	TSR	Observed Value	Fitted Value	Mean Absolute Error
2	0.5	15	3.62	0.98	1.01	0.0448
2.5	2	0	3.16	1.00	1.04	0.0448
1.84	0.5	8.95	3.08	1.17	1.18	0.0448
2.996	0.5	7.11	3.05	1.205	1.204	0.0448
2	0.5	15	3	1.26	1.24	0.0448
1.885	1.85	3.30	3.11	1.10	1.13	0.0448
2	0.5	9	3	1.27	1.29	0.0448

6.3 Optimization of C_p/C_o to Maximize Performance

The projected response surface, illustrated in Figure 14, defines the contour plots (iso-response curves) that provide an adequate representation of most continuous surfaces over a relatively broad factor domain. The combinations of factor levels necessary to achieve the optimal fitted value (maximizing C_p/C_o) is designated over the indicated region by a cross sign and is located at the intersection point of the vertical and horizontal lines (displayed on Figure 14).

In fact, in order to maximize the wind turbine's performance and to reach the highest predicted level of C_p/C_o of 1.29, the operating parameters should be fixed at the following optimal levels: 1.9 to 2 mm for Δx, 0.5 mm for Δy, 9 degrees as δ_f, and 3 as a TSR. While testing these optimal conditions, the observed C_p/C_o that was obtained was 1.27 for the 2D model (shown in Table 7) and 1.19 for the 3D model, the fact that shows that the generated model is valid and presents a high goodness of fit (fitted and observed values were very close, within the MAE range). For further analysis, the slotted turbine model with the combination of design parameters ($\Delta x = 2$ mm, $\Delta y = 0.5$ mm, $\delta_f = 9^0$, TSR = 3) that yields optimum turbine performance will be known as the Optimum Case (OC) slotted turbine.
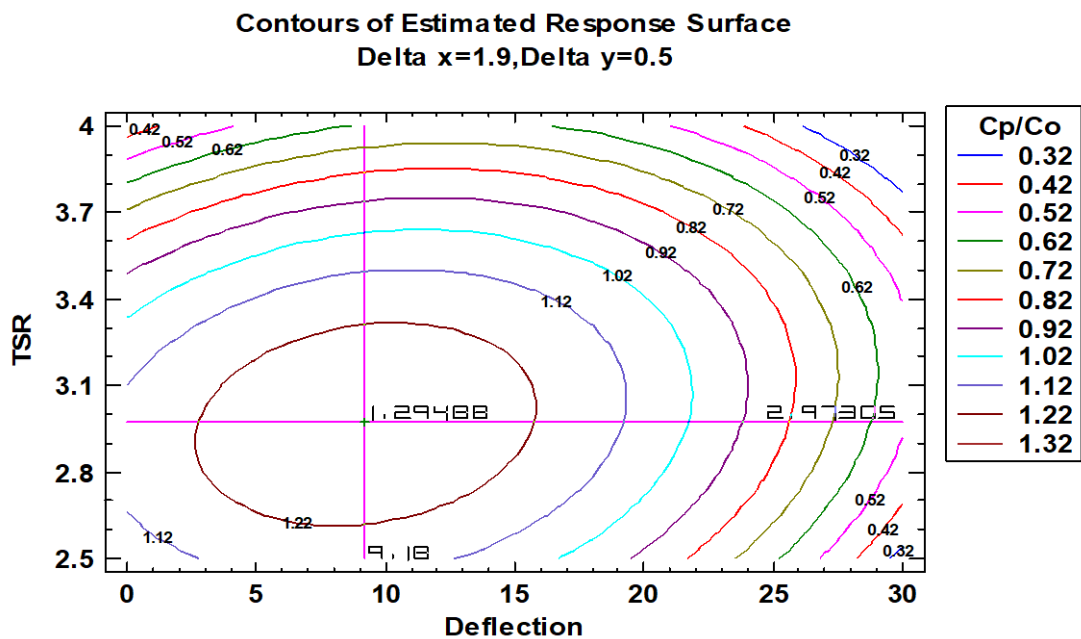

Figure 14: Contour plots of response surfaces and optimum values of operating parameters (Δx, Δy, δf, and TSR) that maximize turbine's performance (Cp/Co) within the test range.

28

6.4 Flow Structure Analysis

Figure 15 shows the 2D case baseline and OC slotted airfoil turbine instantaneous moment coefficient during the turbine first and second halves of the final revolution at TSR 3. As shown in Figure 15 (a), the peak in C_m shifted from $\theta \approx 70^0$ to 90^0 when the optimized case slotted airfoil was utilized. This shift is due to the delayed stall on the blade [29]. Moreover, the sudden reduction in C_m at $70^0 < \theta < 132^0$ for the baseline turbine was noticeably reduced when the optimized case slotted airfoil was applied, and as shown in Figure 15 (b), 64.3% of the C_m curve for the turbine with the OC slotted airfoil lies above that of the baseline turbine. This substantial improvement due to the slotted flap at the trailing edge enhanced the 2D turbine's C_p by 27 %.
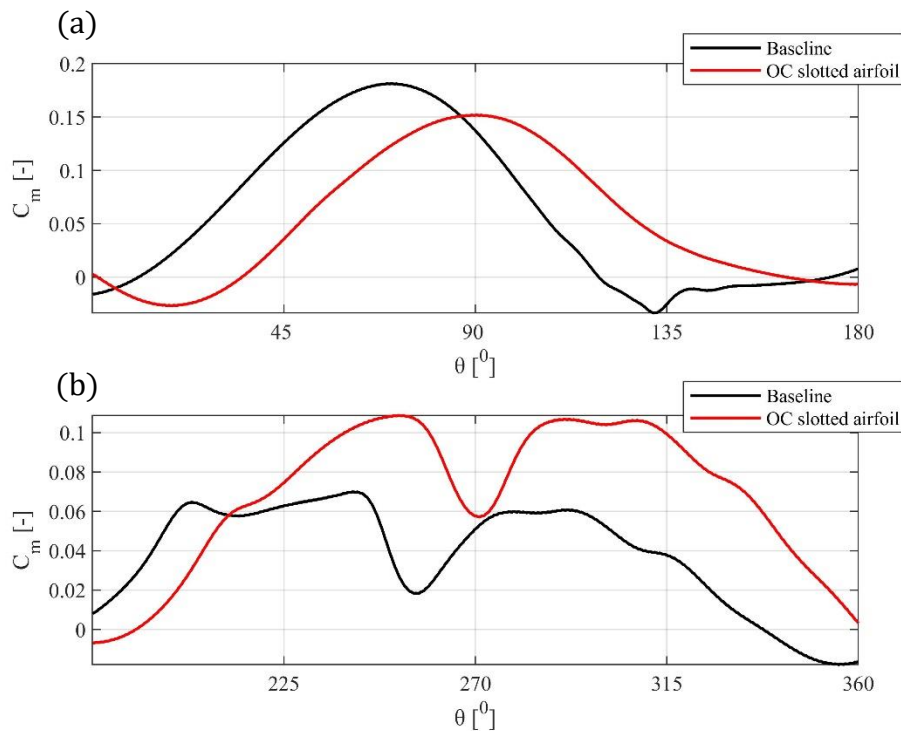
Figure 15: 2D case baseline and OC slotted airfoil instantaneous moment coefficient during the turbine (a) first half revolution and (b) second half revolution at TSR 3

The purpose of this study was to improve the performance of the VAWT by focusing on enhancing the power coefficient. Since this is a lift turbine, not only does the power coefficient improve but so does the flow separation on the turbine blades. By developing the slotted trailing-edge flap, the aim was to encourage the flow fields to closely follow the airfoil profile, and therefore delay as much as possible the early separation of the flow and reduce the size of the wake.

Figure 16: Comparison between 2D vorticity contours for (a) baseline airfoil and (b) the OC slotted airfoil at TSR 3 for $\theta = 0^0$, 45^0, 90^0, 135^0, 180^0, 225^0, 270^0, and 315^0

Figures 16 and 17 illustrate the flow separation phenomena through the visualization of the vorticity and velocity contours, respectively. The contours were generated for the baseline and OC slotted airfoil at TSR 3 for a complete rotation starting at $\theta = 0^0$ and following with 45^0 increments. The observations made are as follows:

30

- At $\theta = 0^0$, compared to the baseline, the slotted airfoil seems to exhibit a somewhat thicker wake with a slight detachment at the trailing edge.
- At $\theta = 45^0$, unfortunately the flow separation commenced earlier on the blade's suction surface with the application of the slotted airfoil. This would
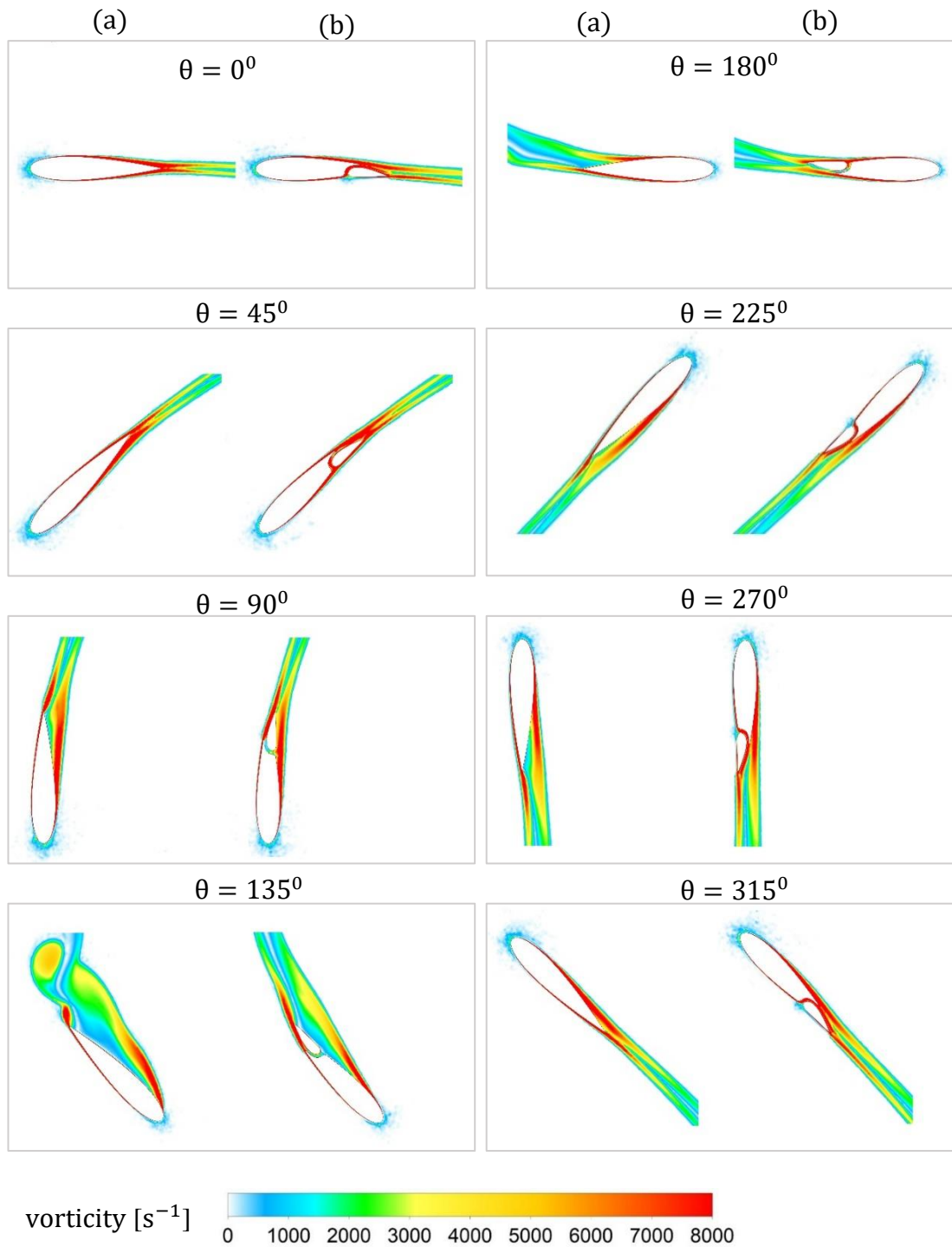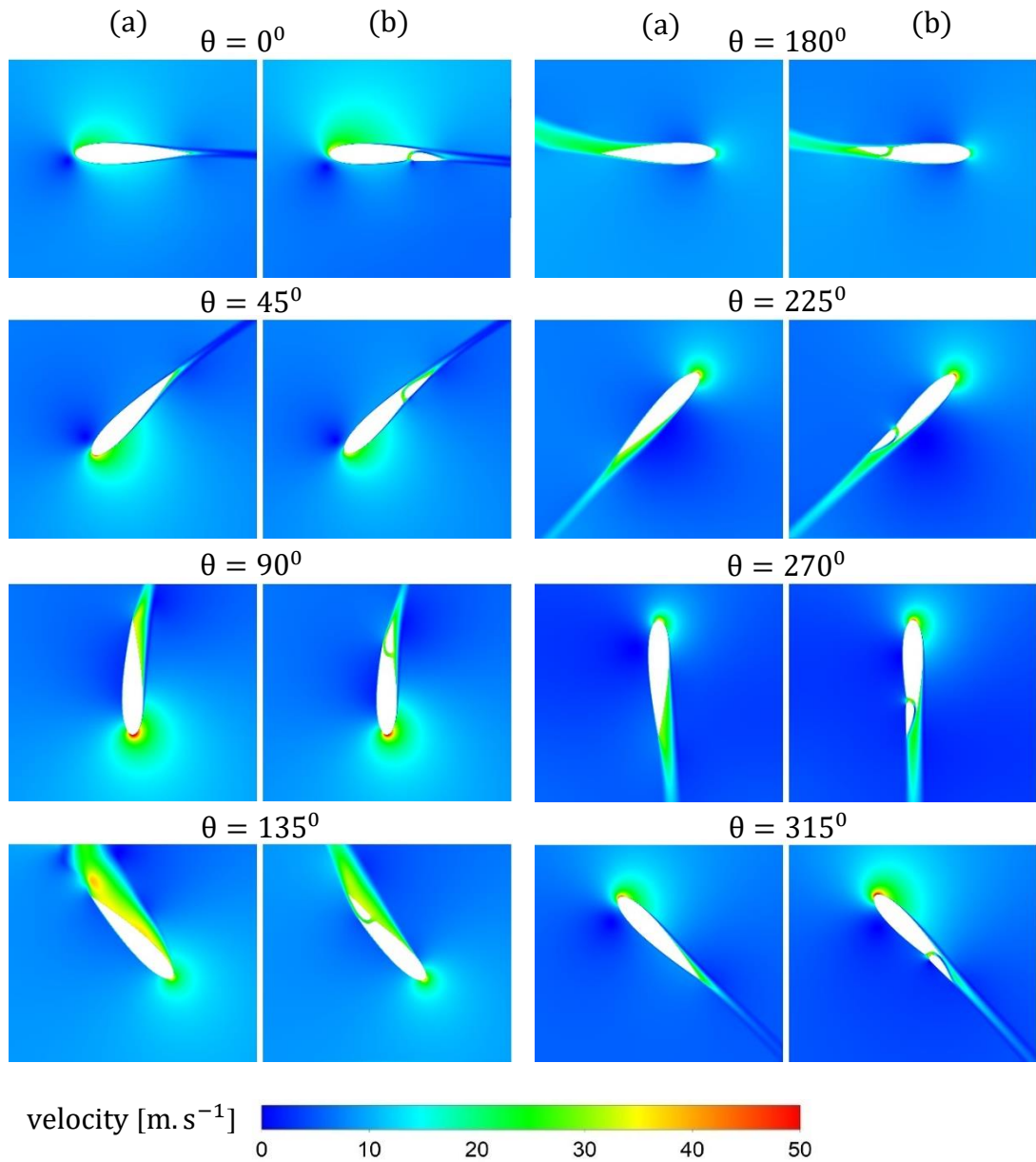

Figure 17: Comparison between 2D velocity contours for (a) baseline airfoil and (b) the OC slotted airfoil at TSR 3 for $\theta = 0^0$, 45^0, 90^0, 135^0, 180^0, 225^0, 270^0, and 315^0

explain the lower value of C_m exhibited by the OC slotted airfoil at this azimuth location as shown in Figure 15.
- At $\theta = 90^0$, improvement becomes noticeable where the slotted airfoil demonstrates a thinner boundary layer separation and delayed flow

31

separation. The vorticity is slightly starting to destabilize at this azimuth angle for the baseline, whereas that of the slotted airfoil still exhibits stable vorticity. The trailing-edge vortex curled down with respect to the chord when the slotted flap was employed, which indicates a reduction in flow reversal and stall. This observation is in perfect agreement with the increase in the C_m value presented at this orientation when the OC slotted airfoil is utilized as depicted in Figure 15.

- At $\theta = 135^0$, the performance enhancement becomes even more prominent where the slotted airfoil exhibits an obvious reduction in wall shear thickness and a delay in flow separation. The formation of a leading-edge vortex (LEV) on the surface of the baseline blade appears at this orientation but has been successfully pushed backwards with the slotted flap in place. The slotted airfoil still shows stable vorticity and velocity profiles with a visible trailing-edge vortex sheet, whereas the baseline's vorticity shows instability, and the trailing-edge vortex is more curled down when compared to that of the slotted airfoil, thus contributing to the stall. This explains the improvement in C_m exhibited by the OC slotted airfoil at $\theta = 135^0$ as illustrated in Figure 15.

- At $\theta = 180^0$, compared to the baseline, the slotted airfoil shows a thinner shear layer. The vorticity profile is more stable than that of the baseline with better flow attachment. However, the delay of flow separation at the suction of the OC slotted airfoil was unsuccessful and this could explain the lower C_m at $\theta = 180^0$ presented in Figure 15.

- At $\theta = 225^0$, the onset of the flow separation remains unchanged, but the shear wall thickness has decreased, and the vorticity profile of the slotted airfoil is more attached and hence more stable.

- At $\theta = 270^0$, improvement is also noticeable where the slotted airfoil demonstrates a thinner boundary layer separation and delayed flow separation. The trailing-edge vortex of the slotted airfoil curled downwards, which indicates a reduction in stall. Moreover, the vorticity profile of the slotted airfoil is more attached and therefore more stable.

- At $\theta = 315^0$, compared to the baseline, the boundary layer separation has decreased.

As stated, several improvements in the flow fields surrounding the slotted airfoil have been demonstrated. As this is a lift turbine, the aerodynamic performances are interdependent, and thus, as the flow separation is controlled, the load of the wind turbine blade decreases and subsequently increases its overall efficiency. It has been revealed that, at some azimuth positions of the blade, as the fluid field becomes more stable with reduced flow separation, the vorticity also develops stably, and this reduces the vibration and noise generated by the device. Most importantly, this increases the turbine's power extraction, and hence this explains the increase in the slotted-flapped turbine's power coefficient in comparison with that of the baseline.

Figure 18 illustrates 3D velocity contours on iso-surfaces of Q-criterion = 5000. The contours were generated for the baseline and OC slotted airfoil at TSR 3 for a complete rotation starting at $\theta = 0^0$ and following with 45^0 increments. The isometric views of the VAWT are located on the left side of Figure 18 and the top views are located on the right. It is important to highlight that the appearance of shedding at the trailing edges of the turbine's blades indicate flow detachment. The shedding phenomenon strongly affects the energy extraction capability of vertical axis wind turbines, as it decreases the instantaneous moment coefficient. The turbine blades with slotted flaps experience less shedding, less detachment and hence improved flow characteristics at all orientations illustrated on Figure 18 except those located at $\theta = 0^0$ and 45^0, which is highly acceptable and enough to say that this implementation of a single slotted flap located at the trailing edge of the VAWT has successfully improved the turbine's power coefficient, delayed flow separation, and improved the overall flow profiles bounding the blades.
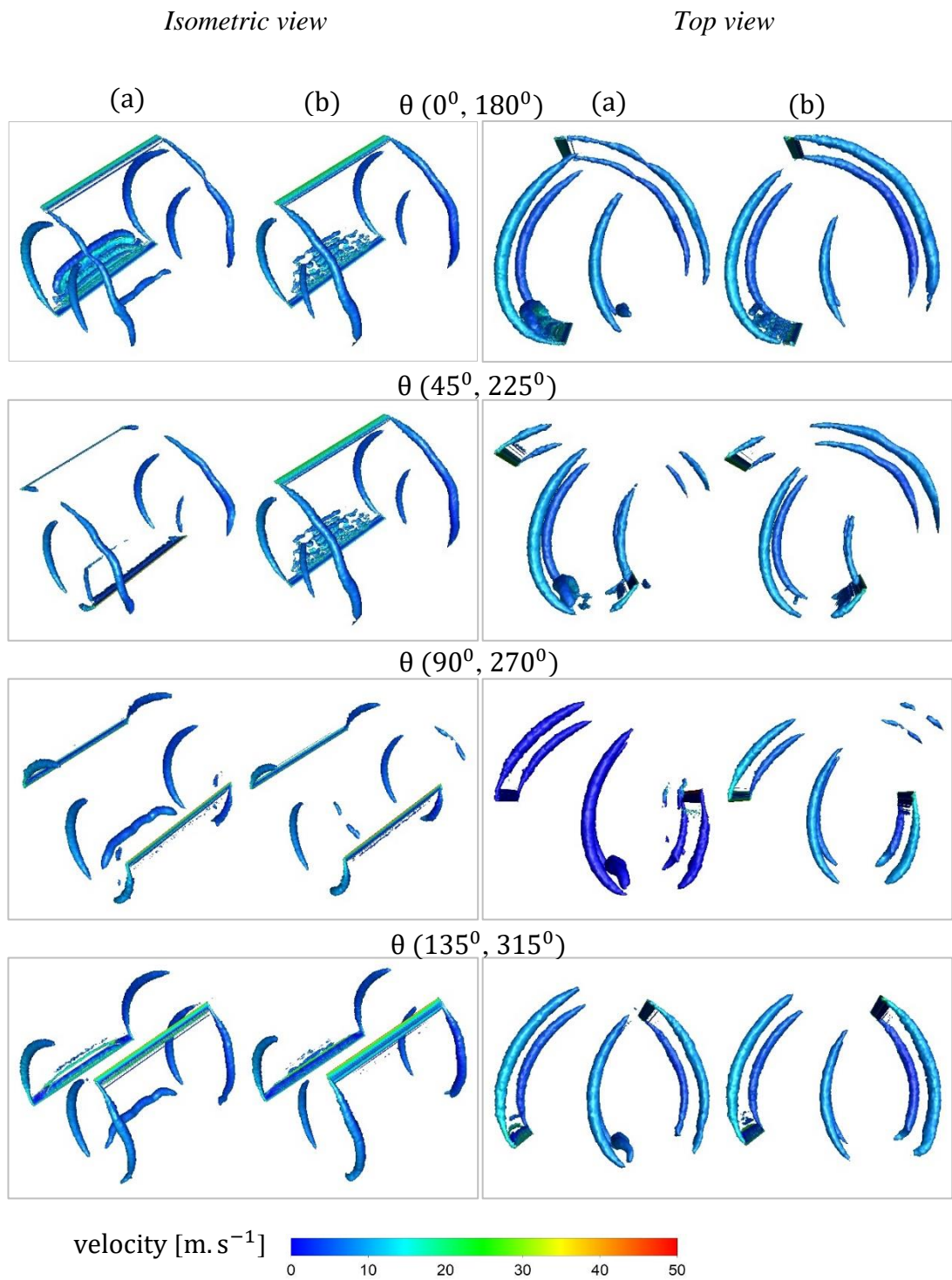
Figure 18: 3D velocity contours on iso-surfaces of Q-criterion = 5000 for (a) baseline airfoil and (b) the OC slotted airfoil at TSR 3 for $\theta = 0^0$, 45^0, 90^0, 135^0, 180^0, 225^0, 270^0, and 315^0

6.5 More on Turbine Performance

Figure 29 presents the DOE model's predicted variation of the optimum C_p/C_o values at TSRs 2 – 4, and their respective design parameters combinations are presented on Table 8. The figure shows that the power coefficient of the slotted turbine is higher than that of the baseline turbine at TSRs 2.5 – 3.5, but this is the opposite at TSRs 2 and 4. The peak power coefficient enhancement is at TSR 3 as expected.
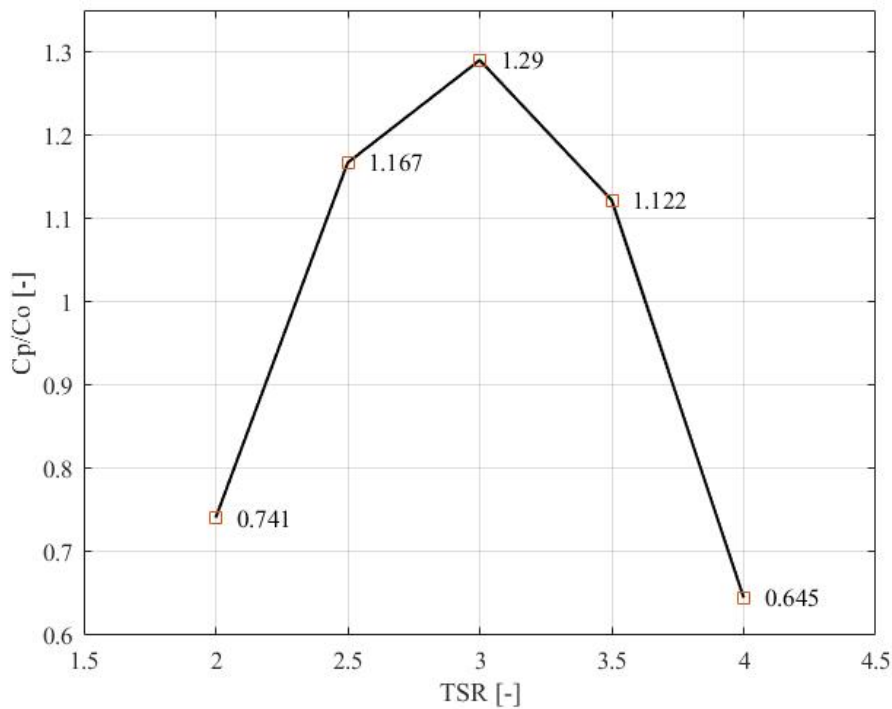
Figure 19: Optimum C_p/C_o vs TSR

Moreover, an analysis on the slotted turbine designed with the OC design parameters at different TSRs was conducted and the corresponding C_p/C_o at different each TSR was noted and presented on Table 9. As shown, the turbine with the OC design parameters exhibits performance improvement at TSRs 2.5, 3, and 3.5 and experiences deterioration in performance at TSRs 2 and 4, and this provides room for wind speed change as the OC slotted turbine will still perform better than the baseline turbine within these ranges (TSR 2.5-3.5).

The deterioration in turbine performance at TSRs 2 and 4 can be explained through Figures 20-23, which shows the flow structure surrounding the turbine blades at $\theta = 135^0$ and $\theta = 180^0$ for the baseline and slotted turbines. With the application of the

slotted design at TSR 2, the flow on the surface of the turbine shows a boundary layer separation which was not as evident on the surface of the baseline turbine at $\theta = 135^0$, and the slotted airfoil shows higher instability and higher vorticity as illustrated on the vorticity contours. At TSR 4, the boundary layer formed over the suction surface of the slotted turbine is thicker and commences earlier when compared to the baseline, and the vortex sheet is thicker than the baseline's at $\theta = 180^0$. This analysis explains the deterioration in the slotted turbine performance at TSRs 2 and 4.

Table 8 Combination of design parameters for optimum C_p/C_o at various TSRs

TSR	Δx	Δy	δ_f	Max. C_p/C_o
2	2.34	0.5	6	0.741
2.5	2.14	0.5	7.8	1.167
3	2	0.5	9	1.290
3.5	1.76	0.5	10.2	1.122
4	1.92	0.5	12.9	0.645

velocity [m. s^{-1}]

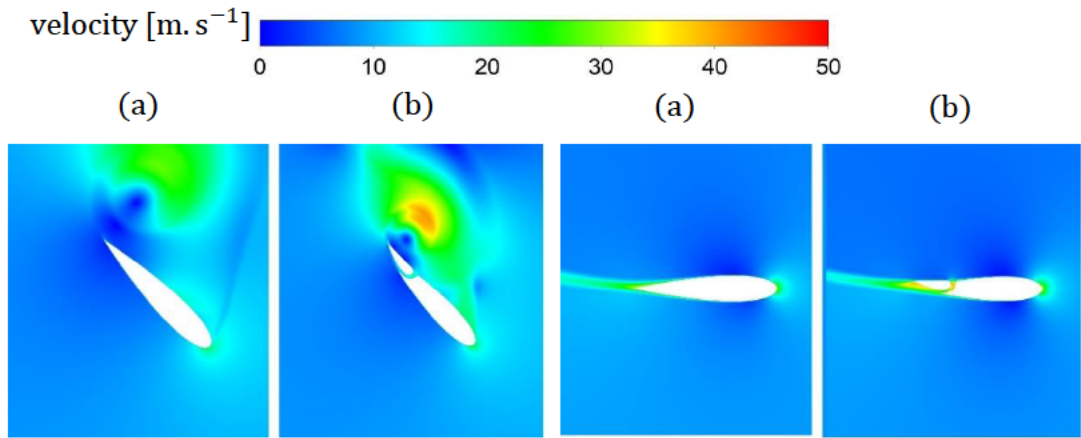|					
0	10	20	30	40	50

(a)　　　　(b)　　　　(a)　　　　(b)

Figure 20: Velocity contours at TSR 2 for (a) baseline airfoil and (b) the OC slotted airfoil at $\theta = 135^0$

Figure 21: Velocity contours at TSR 4 for (a) baseline airfoil and (b) the OC slotted airfoil at $\theta = 180^0$

vorticity [s^{-1}]

0   1000 2000 3000 4000 5000 6000 7000 8000

(a)   (b)   (a)   (b)
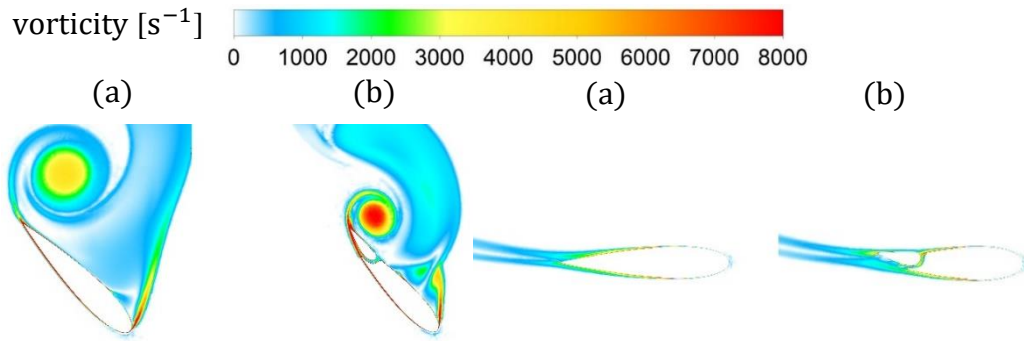
Figure 22: Vorticity contours at TSR 2 for (a) baseline airfoil and (b) the OC slotted airfoil at $\theta = 135^0$

Figure 23: Vorticity contours at TSR 4 for (a) baseline airfoil and (b) the OC slotted airfoil at $\theta = 180^0$

Table 9 C_p/C_o at $\Delta x = 2\ mm, \Delta y = 0.5\ mm, \delta_f = 9^0, TSR = 3$ for various TSRs

TSR	Fitted C_p/C_o
2	0.72
2.5	1.163
3	1.290
3.5	1.113
4	0.619

Chapter VII

Conclusion

The purpose of this study was to enhance the aerodynamic performance of an H-rotor VAWT by employing a slotted deflective flap at the trailing edge of the turbine blades. The DOE method was applied optimize the slot position and to understand the influence of the different design parameters (Δx, Δy, δ_f, TSR) on the performance of the turbine. A 2D numerical study was carried out using CFD to analyse the performance of the slotted airfoil. Thereafter, a 3D numerical study was conducted to further validate the results of the OC slotted airfoil obtained from the 2D run. The OC turbine's power coefficients and flow fields were obtained and analysed. The major findings from this study are summarised as follows:

- The optimum slot position for this low solidity H-rotor was $\Delta x = 2$ mm, $\Delta y = 0.5$ mm, and $\delta_f = 9^0$ at TSR 3.
- The optimized VAWT displayed a 27% and a 17% power enhancement at a TSR of 3 for the 2D and 3D models, respectively.
- The DOE method in association with CFD was a very effective tool to optimize the slot position for this VAWT.
- The flap's deflection angle and TSR had the greatest impact on the slotted turbine's performance. While increasing the deflection from 0 to 30 degrees, the wind turbine performance drastically decreased. TSR had a significant positive linear effect with a clearly noticeable negative quadratic effect on turbines' performance with the best C_p/C_o being achieved at a TSR of around 3.
- The application of the deflected slot on the airfoil blade enhanced the turbine's power coefficient at TSRs 2.5 – 3.5, and the turbine's peak C_p/C_o was found at TSR 3.
- The slotted turbine with the OC design parameters can be exposed to wind speed changes and still perform better than the baseline withing a TSR range of 2.5-3.5.
- The slotted airfoil effectively delayed the boundary layer separation as the pressure difference between both ends of the slot caused a jet flow to pass through the suction side of the airfoil at certain azimuth positions, generating

a high momentum flow injected into the boundary layer on the upper surface which controlled the flow separation.

- The vorticity distribution showed that the presence of a slotted deflective flap at the trailing edge of a VAWT alleviated vortices shedding considerably, which enhanced the turbine's energy extraction capability.

Hence, this study showed that employing CFD and DOE methods is an effective approach to optimize an H-rotor VAWT with several design parameters as this method is very time-efficient. The interactions among the design and dependent variables can be identified and analysed to obtain the optimized design. This study promotes energy-saving benefits through the improvement of the VAWT's efficiency. Additionally, it provides an upgrade in the wind energy market, creating a stride forward in the overall renewable energy industry while adding to the knowledge of science and engineering. Finally, it is important to mention that future works should aim to focus on a wind tunnel experimental study on the OC slotted airfoil turbine.

References

[1] J. Lee and F. Zhao, "Global Wind Report 2019," Brussels, 2020.

[2] E. Möllerström, P. Gipe, J. Beurskens, and F. Ottermo, "A historical review of vertical axis wind turbines rated 100 kW and above," *Renewable and Sustainable Energy Reviews*, vol. 105. Elsevier Ltd, pp. 1–13, May 01, 2019. doi: 10.1016/j.rser.2018.12.022.

[3] M. Khudri Johari, M. Azim A Jalil, and M. Faizal Mohd Shariff, "Comparison of horizontal axis wind turbine (HAWT) and vertical axis wind turbine (VAWT)," *International Journal of Engineering & Technology*, vol. 7, no. 4.13, p. 74, Oct. 2018, doi: 10.14419/ijet.v7i4.13.21333.

[4] H. Zhu, W. Hao, C. Li, and Q. Ding, "Effect of flow-deflecting-gap blade on aerodynamic characteristic of vertical axis wind turbines," *Renewable Energy*, vol. 158, pp. 370–387, Oct. 2020, doi: 10.1016/j.renene.2020.05.092.

[5] J. Martinez Suarez, P. Flaszynski, and P. Doerffer, "Application of rod vortex generators for flow separation reduction on wind turbine rotor," *Wind Energy*, vol. 21, no. 11, pp. 1202–1215, Nov. 2018, doi: 10.1002/we.2224.

[6] H. Wang *et al.*, "Effects of leading edge slat on flow separation and aerodynamic performance of wind turbine," *Energy*, vol. 182, pp. 988–998, Sep. 2019, doi: 10.1016/j.energy.2019.06.096.

[7] Q. Liu, W. Miao, C. Li, W. Hao, H. Zhu, and Y. Deng, "Effects of trailing-edge movable flap on aerodynamic performance and noise characteristics of VAWT," *Energy*, vol. 189, Dec. 2019, doi: 10.1016/j.energy.2019.116271.

[8] H. Shan, L. Jiang, C. Liu, M. Love, and B. Maines, "Numerical study of passive and active flow separation control over a NACA0012 airfoil," *Computers & Fluids*, vol. 37, no. 8, pp. 975–992, Sep. 2008, doi: 10.1016/j.compfluid.2007.10.010.

[9] R. Raju, E. Aram, R. Mittal, and L. Cattafesta, "Simple Models of Zero-Net Mass-Flux Jets for Flow Control Simulations," *International Journal of Flow Control*, vol. 1, no. 3, pp. 179–197, Sep. 2009, doi: 10.1260/175682509789877092.

[10]   D. Luo, D. Huang, and X. Sun, "Passive flow control of a stalled airfoil using a microcylinder," *Journal of Wind Engineering and Industrial Aerodynamics*, vol. 170, pp. 256–273, Nov. 2017, doi: 10.1016/j.jweia.2017.08.020.

[11]   Y. Yang, C. Li, W. Zhang, X. Guo, and Q. Yuan, "Investigation on aerodynamics and active flow control of a vertical axis wind turbine with flapped airfoil," *Journal of Mechanical Science and Technology*, vol. 31, no. 4, pp. 1645–1655, Apr. 2017, doi: 10.1007/s12206-017-0312-0.

[12]   O. S. Mohamed, A. A. Ibrahim, A. K. Etman, A. A. Abdelfatah, and A. M. R. Elbaz, "Numerical investigation of Darrieus wind turbine with slotted airfoil blades," *Energy Conversion and Management: X*, vol. 5, Jan. 2020, doi: 10.1016/j.ecmx.2019.100026.

[13]   P. Sforza, "Wing Design," in *Commercial Airplane Design Principles*, Elsevier, 2014, pp. 119–212. doi: 10.1016/B978-0-12-419953-8.00005-X.

[14]   D. Florjancic, "Improved Design of a High Lift System for General Aviation Aircraft," Netherlands, 2015.

[15]   W. LU, Y. TIAN, and P. LIU, "Aerodynamic optimization and mechanism design of flexible variable camber trailing-edge flap," *Chinese Journal of Aeronautics*, vol. 30, no. 3, pp. 988–1003, Jun. 2017, doi: 10.1016/j.cja.2017.03.003.

[16]   G. Tescione, D. Ragni, C. He, C. J. Simão Ferreira, and G. J. W. van Bussel, "Near wake flow analysis of a vertical axis wind turbine by stereoscopic particle image velocimetry," *Renewable Energy*, vol. 70, pp. 47–61, Oct. 2014, doi: 10.1016/j.renene.2014.02.042.

[17]   A. Rezaeiha, H. Montazeri, and B. Blocken, "Towards accurate CFD simulations of vertical axis wind turbines at different tip speed ratios and solidities: Guidelines for azimuthal increment, domain size and convergence," *Energy Conversion and Management*, vol. 156, pp. 301–316, Jan. 2018, doi: 10.1016/j.enconman.2017.11.026.

[18]   C. S. Ferreira, "The near wake of the VAWT 2D and 3D views of the VAWT – 2D and 3D views of the VAWT aerodynamics." 2009.

[19] F. Balduzzi, A. Bianchini, R. Maleci, G. Ferrara, and L. Ferrari, "Critical issues in the CFD simulation of Darrieus wind turbines," *Renewable Energy*, vol. 85, pp. 419–435, Jan. 2016, doi: 10.1016/j.renene.2015.06.048.

[20] Z. Wang, Y. Wang, and M. Zhuang, "Improvement of the aerodynamic performance of vertical axis wind turbines with leading-edge serrations and helical blades using CFD and Taguchi method," *Energy Conversion and Management*, vol. 177, pp. 107–121, Dec. 2018, doi: 10.1016/j.enconman.2018.09.028.

[21] R. Bontempo, R. Carandente, and M. Manna, "A design of experiment approach as applied to the analysis of diffuser-augmented wind turbines," *Energy Conversion and Management*, vol. 235, May 2021, doi: 10.1016/j.enconman.2021.113924.

[22] M. Ahmad, A. Shahzad, F. Akram, F. Ahmad, and S. I. A. Shah, "Design optimization of Double-Darrieus hybrid vertical axis wind turbine," *Ocean Engineering*, vol. 254, Jun. 2022, doi: 10.1016/j.oceaneng.2022.111171.

[23] J. Tang, F. Avallone, R. Bontempo, G. J. W. van Bussel, and M. Manna, "Experimental investigation on the effect of the duct geometrical parameters on the performance of a ducted wind turbine," in *Journal of Physics: Conference Series*, Jun. 2018, vol. 1037, no. 2. doi: 10.1088/1742-6596/1037/2/022034.

[24] S. Acarer, Ç. Uyulan, and Z. H. Karadeniz, "Optimization of radial inflow wind turbines for urban wind energy harvesting," *Energy*, vol. 202, Jul. 2020, doi: 10.1016/j.energy.2020.117772.

[25] P. F. S. Trentin, P. H. B. de B. Martinez, G. B. dos Santos, E. E. Gasparin, and L. O. Salviano, "Screening analysis and unconstrained optimization of a small-scale vertical axis wind turbine," *Energy*, vol. 240, Feb. 2022, doi: 10.1016/j.energy.2021.122782.

[26] T. tian Zhang *et al.*, "Winglet design for vertical axis wind turbines based on a design of experiment and CFD approach," *Energy Conversion and Management*, vol. 195, pp. 712–726, Sep. 2019, doi: 10.1016/j.enconman.2019.05.055.

[27]   S. Torres, A. Marulanda, M. F. Montoya, and C. Hernandez, "Geometric design optimization of a Savonius wind turbine," *Energy Conversion and Management*, vol. 262, Jun. 2022, doi: 10.1016/j.enconman.2022.115679.

[28]   A. M. Hwas Lect and A. M. Hatab, "Effects of Design Parameters of Wind Turbine on Airfoil Coefficients Using Grey-Based Taguchi Method," 2020. [Online]. Available: www.jmest.org

[29]   A. Rezaeiha, H. Montazeri, and B. Blocken, "CFD Investigation of Separation Control on a Vertical Axis Wind Turbine: Steady and Unsteady Suction," in *Journal of Physics: Conference Series*, Sep. 2020, vol. 1618, no. 5. doi: 10.1088/1742-6596/1618/5/052019.